A synoptic view of mantle plume shapes enabled by virtual reality

Qianyi Lu, Maxwell L. Rudolph[1]

[1]Department of Earth and Planetary Sciences, University of California, Davis, Davis, CA, USA

Key Points:

- The variation of shear velocity anomaly along the traced conduits suggests a thermochemical origin of most of the plumes.
- We identify complex plume shapes (ponding, branching, and merging) that suggest complex rheological structure of the lower mantle.
- We provide systematic and quantitative observations of plume shapes that can benefit numerical modeling and geochemical studies of plumes.

Corresponding author: Qianyi Lu, ayylu@ucdavis.edu

Abstract

The shapes of mantle plumes are sensitive to mantle viscosity, density structure, and flow patterns. Increasingly, global tomographic models reveal broad plume conduits in the lower mantle and highly sheared conduits in the mid and upper mantle. Previous studies mostly relied on 2D slices to analyze plume shapes, but as plume conduits are 3D structures, this approach falls short of fully capturing their complexity. Here, we use immersive virtual reality (VR) headsets to visualize the full-waveform global tomographic models SEMUCB-WM1 and GLAD-M25. We develop criteria for the identification of plume conduits based on the relationship between the plume excess temperature and the V_S anomaly (δV_S) to trace plume conduits from these tomographic models. We are able to trace 20 major plume conduits, measure the offsets of the conduits in azimuth and distance with respect to the hotspots, calculate the tilted angle, and evaluate the δV_S along all traced conduits. We compare our traced conduits with the conduits predicted by global mantle convection models and vertical conduits. Our traced conduits from SEMUCB-WM1 and GLAD-M25 are slower than the modeled conduits and vertical conduits whether they are evaluated in the same tomographic model or a different tomographic model. The shapes of traced conduits tend to differ greatly from modeled conduits. Plume ponding and the emergence of secondary plumes, which could result from a combination of different plume compositions, phase transitions, small-scale convection, and variations in viscosity and density of the ambient mantle, can contribute to the complex observed plume shapes.

1 Introduction

Deep mantle plumes originating from the Core Mantle Boundary (CMB) are thought to have a broad head, which generates Large Igneous Provinces (LIPs), and a narrower tail, which forms long-lived hotspots (e.g. Richards et al., 1989). The geochemical diversity of hotspot lavas, which are also known as Ocean Island Basalts (OIBs), reflects the entrainment and transport of different mantle materials by ascending plumes. Hence, understanding the shapes of mantle plumes is important for linking the rock record with deep mantle structures, including the Large Low Shear Velocity Provinces (LLSVPs) and Ultra Low Velocity Zones (ULVZs). Plume shape is influenced by the global pattern of mantle circulation as well as the intrinsic buoyancy and viscosity variations within ascending plumes and the ambient mantle. Seismic tomography is the only geophysical method that currently resolves plume-scale features at all mantle depths. Tomographic models shape our understanding of mantle plumes and naturally become a constraint on numerical models that aim to understand their structure and evolution. These comparisons bridge our theoretical models to tomographic images of mantle plumes and help advance our understanding of the physical and chemical properties of mantle plumes. Here we analyze the shapes of mantle plumes using immersive 3D visualization based on two recent global tomographic models and consider the implications of plume shape for the pattern of global mantle circulation and the variation of mantle viscosity.

Mantle plumes that rise to the surface have previously been described conceptually as primary and secondary plumes (Courtillot et al., 2003) on the basis of their buoyancy fluxes, upper mantle seismic signature, and the isotopic variations in OIBs. Primary plumes rise directly from the CMB, whereas secondary plumes rise from the superswells or broad primary plumes that pond below the upper mantle. State-of-art global tomographic models show patterns of slow shear velocity (Vs) resembling both types of plumes, although the plume shapes revealed by tomographic models have more complexities than what is proposed by the schematic plume model of Courtillot et al. (2003).

There has been considerable debate about whether hotspots are preferentially located at the edges of the Pacific and African LLSVPs (Torsvik et al., 2006; Steinberger & Torsvik, 2012) or whether they are associated with the LLSVP edges and interiors (Austermann

et al., 2014; Davies et al., 2015; Doubrovine et al., 2016). These two hypotheses have different geodynamics implications: whether plumes rise from the edge of the pile-like LLSVPs (Tan et al., 2011; Hassan et al., 2015), or the LLSVPs are cluster of plumes (Davaille & Romanowicz, 2020).

Two complementary approaches have been taken to understand the evolution of mantle plumes. First, some numerical models of thermal and thermochemical plume ascent focus on idealized plumes and incorporate a high degree of physical realism at the expense of describing the geologic context of specific plumes within Earth's mantle (Dannberg & Sobolev, 2015; H. Liu & Leng, 2020). A second class of numerical models focuses on the influence of global mantle flow that are consistent with Earth's tectonic history on modeled plume conduits at the expense of a complete treatment of mantle rheology, phase transitions, and plume buoyancy (e.g., Steinberger & O'Connell, 1998). For the first class of study, the comparison between the shape of the observed and the modeled plume conduits is only qualitative because idealized models do not attempt to reproduce the detailed dynamics of specific plumes. The second class of models does make testable predictions of plume shape that can be qualitatively and quantitatively compared with plumes resolved in tomographic models but only in terms of the wavespeed variations (Boschi et al., 2007).

Plume shapes depend on both the inherent properties of a plume and the surrounding mantle conditions, so they provide information about the composition and dynamics of plume and mantle. For example, the amount and direction of shear of plume conduits reflect the large-scale mantle flow pattern. Changes in the conduit radius could indicate the viscosity variations across the mantle. The stagnation of plumes helps to reveal the influence of the pressure-induced phase transitions on mantle convection. It is crucial to measure the shapes of plume conduits quantitatively to make more appropriate and meaningful connections between numerical models and tomographic observations.

Measuring plume shapes from tomographic models requires effective visualization of what are three-dimensional (3D) datasets, but most approaches to their visualization have involved two-dimensional (2D) slicing or the rendering of isosurfaces (surfaces defined by a constant value) on a 2D medium such as a computer screen or a paper (S. French & Romanowicz, 2015; Tsekhmistrenko et al., 2021; Celli et al., 2021). The understanding and insight gained from 2D visualizations of 3D data may be different than that gained through immersive 3D visualization. For example, the 2D cross-section of a plume cluster associated with the Pacific LLSVP seems to imply that the conduits of plume Samoa, and Tahiti are not resolved above 660 km depth (Figure 1a). However, the conduits of these plumes extend out of the vertical cross-section plane, as shown in Figure 1b. Selecting an isosurface with a specific negative δV_S to represent the boundary of a plume reveals plume shapes better than 2D cross sections and allows us to "see through" the non-negative δV_S that obscures our view. However, these approaches may fail if the shape of a plume is best represented by different isosurface values at different depths or when many plumes are clustered. In the first case, visualizing plumes requires observing the structures of many different δV_S isosurfaces simultaneously. In the second case, the isosurfaces representing boundaries of conduits usually obscure each other, making it tricky to identify an individual conduit if the observer is outside the cluster. This is the scenario for the plumes feeding Pitcairn, Macdonald, Marquesas, Tahiti, Samoa, and Easter, which are located close together within the Pacific LLSVP (Figure 2).

Visualizing seismic tomographic models in a virtual reality (VR) environment can help to overcome these barriers. Immersive visualization allows an observer to explore inside mantle structures and view them quickly from arbitrary vantage points. Immersive 3D visualization is not new in geoscience research but has not seen widespread adoption due to the lack of commodity VR hardware and related software. Previously, the usage of VR environments centered on large, immobile, and expensive "cave" environments (e.g., Billen et al., 2008). As VR heatset devices have become more prevalent,

immersive 3D visualization is becoming more accessible due to its lower cost and greater portability, presenting the potential to enable new discoveries.

The remainder of the paper is structured as follows. We establish a quantitative procedure to define mantle plume conduits and discuss the advantages and limitations of our conduit-choosing criteria. We present our traced conduits for well-resolved plumes in SEMUCB-WM1 (S. W. French & Romanowicz, 2014) and GLAD-M25 (Lei et al., 2020) and the quantitative measurement of these conduits. We demonstrate that our traced conduits are more consistent with the distributions of slow seismic velocities than geodynamic model predictions. We discuss the implications and potential applications of this study.

2 Methods

The two tomographic models analyzed in this study, SEMUCB-WM1 and GLAD-M25, are state-of-art global tomographic models based on full waveform inversion (FWI). SEMUCB-WM1 inverts for 3-D variations in Voigt-average isotropic V_S and radial anisotropy parameter ξ and parameterizes them radially using (continuous) cubic b-splines and laterally using spherical splines. Its starting model is SEMum2 (S. French et al., 2013) above 800 km and SAW24B16 (Mégnin & Romanowicz, 2000) below. The crust is approximated by a smooth anisotropic layer to account for the crustal effects on wave propagation and dispersion. GLAD-M25 inverts for the bulk sound speed and vertically and horizontally polarized V_S in the mantle above 660 km. Its starting model is S362ANI (Kustowski et al., 2008) for the mantle and Crust2.0 (Bassin et al., 2000) for the crust. As in the starting model S362ANI, GLAD-M25 uses a parameterization that includes first- and second-order discontinuities in the radial direction, permitting abrupt changes in the pattern of heterogeneity across the mantle transition zone. Both of the global tomographic models resolve broad plumes rising from the CMB to the upper mantle beneath many hotspots (S. French & Romanowicz, 2015; Lei et al., 2020).

We define plume conduits based on three considerations. *First*, we require plume conduits to be continuous pathways from the lithosphere to the CMB. *Second*, we require that plume conduits be slower than average across all mantle depths (i.e., having a negative δV_S). *Third*, we seek plume conduits for which the temperature anomaly implied by wave speed variations is consistent with petrological constraints on plume excess temperature. The third criterion may not always be satisfiable due to limitations in tomographic modeling, discussed later.

Following our criteria, we manually traced the conduits of 20 plumes (listed in Table S1), of which the buoyancy flux is larger than 1000 kg/s (Jackson et al., 2021) and are well-resolved in both SEMUCB-WM1 and GLAD-M25. We exclude the Yellowstone plume as it is only well-resolved in GLAD-M25. We include the Canary and St. Helena plumes, of which the buoyancy flux is only 800 and 500 kg/s, respectively, because similar plume shapes are clearly resolved in both tomographic models. Moreover, the OIBs associated with both hotspots display isotopic signatures supporting a deep mantle origin.

The plume conduits are traced in a headset-based immersive 3D visualization environment. We use the Valve Index VR headset and controllers and the Paraview 5.10.0 (Ahrens et al., 2005) visualization software. The identification of plume conduits was carried out using the following steps:

1. The traced conduit (TC) of each plume can be divided into an upper-mantle, a mid-mantle, and a lower-mantle part. We first identify candidate conduits (CCs) - conduit-like vertical negative δV_S structures - that extend vertically across the mid mantle near each surface hotspot. There may be multiple candidate conduits

for each hotspot, and we seek conduits that are closer to the hotspot's surface expression.

2. We use pipelines (control points connected by line segments) to represent the pathway of the traced conduit, where the control points are assigned every 200 km from 250 to 2450 km depth. We seek an upper-mantle TC, which connects the surface hotspot with the upper-end of the mid-mantle TC, and a lower-mantle TC, which starts from the lower-end of the mid-mantle TC. Where there is ambiguity, we prefer more vertical plume conduits.
3. After tracing the plume conduits, we validate our TCs according to two criteria. First, the δV_S along a TC should not be positive. Second, we use the plume and ambient mantle potential temperature calculated from olivine-liquid equilibria (Putirka, 2008) to estimate the excess temperature of plumes. We then calculate the profile of $d(\ln V_S)/dT$ (Figure S1) assuming that the plume has a pyrolitic composition and use the profile of $d(\ln V_S)/dT$ to calculate δV_S corresponding to the petrologically-estimated excess temperature at all depths for each plume that has an estimation. δV_S along the TC should be comparable to δV_S converted from the petrologically-estimated excess temperature at some depths above 1250 km. The second criterion is not hardwired because the variable resolution, parameterization, and regularization of global tomographic models can all contribute to modeled V_S variations.

3 Results

We describe the general properties of the traced plume conduits (Figure 2), starting from describing the slowness of the traced conduits. We then describe overall trends in the amount of offset from the surface location, the tilt (measured in degrees away from the vertical) of plume conduits, and the depths at which large offsets or tilts occur. We describe the shapes of individual plume conduits in greater detail later.

3.1 Slowness along plume conduits

The δV_S along conduits traced from SEMUCB-WM1 and GLAD-M25 is generally between 0% and -2%, comparable with each other (Figure 3-4). We find that plumes originating from the African LLSVP is faster than that along plumes stemming from the Pacific LLSVP above $\sim$ 1250 km depth in SEMUCB-WM1 and at all depths in GLAD-M25 (Figure 5b, c, g, h). We also evaluate the average δV_S of conduits traced from SEMUCB-WM1 in GLAD-M25 as well as conduits traced from GLAD-M25 in SEMUCB-WM1 (Figure 5d, e, i, j). When plumes traced in one tomographic model are evaluated in the other tomographic model, the average δV_S along TCs around the Pacific LLSVP remains negative at all depths, while it is negative only in the lower mantle for TCs around the African LLSVP.

3.2 Observed morphology

Tilted angles along the traced conduits generally remain smaller in the lower mantle than in the upper mantle with a few exceptions (Figure 6). For example, the Louisville and Azores plumes have a tilted angle (60 – 70°) below 2000 km in SEMUCB-WM1. A comparison of the tilted angles of plumes (Figure 6) and the offsets of plume conduits (azimuth and distance, shown in Figure 7) shows that large tilted angles are associated with abrupt changes in offset distances and/or azimuths of TCs. Changes in offset azimuths and distances are small where the tilt is closer to vertical. The azimuth of a conduit is measured by assuming its hotspot as the origin, 0 degree at the north, and counting clock-wise. Due to the manual process of conduit tracing, the uncertainty in tilt of TCs is at least 5°. Hence TCs with tilt less than this should be interpreted as nearly vertical.

Plume conduits traced in SEMUCB-WM1 and GLAD-M25 usually root at locations offset from their surface hotspots by 5 – 10° and most of the offset occurs in the upper mantle. A few plume conduits show larger offsets. The TCs of Galapagos, San Felix, and Tahiti root at locations offset from their surface hotspots by more than 10° in both tomographic models (Figure 2 and 7). The offsets of conduits traced from SEMUCB-WM1 in the upper mantle can easily exceed 5 degrees (Figure 7), which converts to > 500 km offsets, while those of conduits traced from GLAD-M25 appear to be much smaller.

3.2.1 Paired plumes

In SEMUCB-WM1, the MacDonald and Pitcairn plumes seem to branch from the same conduit in the lower mantle and the Macdonald plume is significantly sheared at $\sim$ 1250 km depth (Figure 8a). The Canary and Cape Verde plumes also appear to share the same conduit from the CMB to at least $\sim$ 1250 km depth and branch into two conduits separated by $\sim$ 15°in the upper mantle (Figure 8b).

In GLAD-M25, we identify CC with a similar shape as what is observed in SEMUCB-WM1 below the Canary and Cape Verde hotspots. We interpret Canary and Cape Verde as two adjacent plumes rising parallel to each other though this CC could be interpreted as either two separate conduits or one broad plume branching into two secondary plumes as it crosses the 660 km discontinuity. CCs of the Pitcairn and Macdonald plumes look less like those in SEMUCB-WM1. These two plumes seem to emerge from different locations at the CMB and merge into a broad plume conduit between 660 and 2000 km depth and branch again above 660 km depth.

The San Felix and Juan Fernandez plumes are another potential paired plumes. These two plumes generally share the same CC in the mid-mantle in both tomographic models (Figure S2). We interpret it as two adjacent plumes rising parallel to each other and trace their conduits based on this interpretation. The conduit of San Felix is not resolved between 1250 and 660 km in SEMUCB-WM1 and above 660 km in GLAD-M25. The conduit of Juan Fernandez is generally well resolved at all depths in both tomographic models.

3.2.2 Iceland

The Iceland plume is generally vertical in both tomographic models, but the detailed shape of the plume is different. Starting from the surface hotspot, the traced conduit from SEMUCB-WM1 is offset towards the northeast above $\sim$ 350 km and then offset back towards the hotspot at $\sim$ 660 km. The conduit remains generally vertical below 660 km and slightly sheared towards the east below $\sim$ 2000 km (Figure 6,7, and 8c). Its TC from GLAD-M25 is vertical above 660 km, sheared first towards the east between 660 and 1000 km depth then towards the west between $\sim$ 1250 and 1500 km depth, and remains vertical below 1500 km.

3.2.3 Hawaii

The Hawaii plume appears to be mostly vertical in SEMUCB-WM1, while it appears to be largely sheared towards the southeast in GLAD-M25. Its conduit is well resolved in SEMUCB-WM1 but not well resolved between 410 and 660 km depth in GLAD-M25 (Figure 8d). Although the TCs from SEMUCB-WM1 and GLAD-M25 are not consistent, both tomographic models resolve a similar CC between 660 and 1250 km depth below the surface hotspot location and a similar CC location at the CMB (Figure 8d).

3.2.4 Samoa, St Helena, Reunion, and Caroline

Similar CCs are identified in both tomographic models for the Samoa, St Helena, Reunion, and Caroline plumes. These plumes remain nearly vertical or slightly tilted in the lower mantle and get sheared more heavily in the upper mantle (Figure 9a-c). We noticed that amplitudes of negative δV_S along these TCs from SEMUCB-WM1 vary smoothly and reach a maximum near 660 km. Amplitudes of the negative δV_S along these TCs from GLAD-M25, however, decrease abruptly above the 660 km discontinuity. These negative δV_S amplitudes are larger (slower) than those of conduits traced from SEMUCB-WM1 by 0.5-1.0 % δV_S below $\sim$ 2000 km (Figure 3 and 4).

3.2.5 Azores, Easter, Galapagos, Kerguelen, Marquesas, and Tahiti

We notice that for the Azores, Easter, Galapagos, Kerguelen, Marquesas, and Tahiti plumes, similar CCs are resolved in the two tomographic models but different TCs are identified (Figure 9d and S3-5). One of the main causes is the poor inter-model agreement above 660 km and below 2000 km. The other main cause is that the δV_S of CCs with similar shapes can amplify at different depths in different tomographic models. It can result in very different interpretations of the most-reasonable conduit path.

4 Discussion

We first demonstrate the reliability of our traced conduits to justify that our TCs represent seismically slow paths through the mantle. We then compare our TCs with modeled conduits and discuss the reasons for their differences. Next, we discuss the implications for mantle and plume dynamics from our observed plume shapes and slowness along conduits. We conclude our discussion by proposing some applications of our TCs in future studies of plume dynamics.

4.1 Reliability of traced conduits

Seismic tomography is a mixed-determined inverse problem, and there exist many possible Earth structures that are equally compatible with seismic observables. Hence, one might question the veracity of mantle plume shapes determined on the basis of seismic tomography. Several lines of evidence suggest that the imaged and traced plume conduits are likely representative of real mantle structures. *First*, the slow V_S structures near many hotspots are similar between the two models, suggesting that the imaged features are robust. *Second*, the average slowness along TCs is much greater than the average slowness along modeled or vertical conduits (Figure 5a-c, f-h). To further assess the robustness of the traced plume conduits, we evaluate the slowness along Pacific TCs obtained from either tomographic model in the other tomographic model. We find that our Pacific TCs are slower than the MCs and vertical conduits (VCs) at $\sim 1250 - 2500$ km depth. This suggests that both sets of traced conduits are more compatible with either tomographic model than the modeled and vertical conduits in the lower mantle. The shapes of plumes could vary between different regional and global tomographic models due to different parameterization/regularization choices and different earthquake events used to constrain the tomographic models (S. French & Romanowicz, 2015; Wamba et al., 2021, 2023).

4.2 Comparison between traced and modeled conduits

Simplified numerical models of mantle plume shapes have been used widely in geodynamics to understand the mobility of deep mantle hotspots and to establish the moving hotspot reference frames necessary for absolute plate reconstructions (e.g., Matthews et al., 2016). We compare modeled conduits (MCs) from (Steinberger & Antretter, 2006)

with our traced conduits. These numerical models of plume dynamics start with a mantle buoyancy structure based on a tomographic model filtered to long wavelength. The buoyancy structure is reconstructed backwards in time through the reversal of buoyancy forces and the application of time-reversed plate reconstructions at the surface while ignoring the effects of thermal diffusion, which cannot be time-reversed due to non-uniqueness. This yields a model of *long-wavelength* (much longer wavelength than the widths of plumes) mantle flow in space and time. Then, initially vertical plume conduits are advected by the flow field forward in time. Previous studies demonstrated that the shapes of MCs are not very sensitive to the tomographic model used to compute the mantle flow field, the details of the plate reconstructions used, or the detailed mantle viscosity structure (Steinberger & O'Connell, 1998; Steinberger, 2000; Steinberger & Antretter, 2006; Williams et al., 2019).

The tilted angles and offsets of MCs show that most of MCs are slightly sheared (tilted angle $< 30°$) below 660 km. This is likely because the deformation rate is slow due to the high viscosity of the lower mantle. Larger tilted angles (up to $> 90°$) of MCs observed above 660 km (Figure 6) are mainly due to the oscillations of the tightly spacing conduit elements in the lower-viscosity upper mantle. The offsets of modeled conduits (shown in Figure 7) show that MCs are in fact sheared gently at these depths. Our TCs suggest that plumes are generally slightly sheared in the lower mantle, but large tilted angles in the mid-mantle below 660 km are observed for many TCs from both tomographic models (e.g., Macdonald, Samoa, St Helena, and Tristan) (Figure 6). TCs generally have more complex shapes than MCs, especially in the mid-mantle.

Although the paths of TCs and MCs are generally not in very good agreement (Figure 2, Table S1), there are a couple of exceptions. TCs of plumes located at the edge of LLSVPs (Canary, Juan Fernandez, San Felix, St Helena, and Reunion)(Figure 7) seem to agree with their MCs better than TCs of plumes located near the center of LLSVPs. Plumes that have similar TCs and MCs have relatively simple shapes, that is, the shear direction of a TC does not change over depths. TCs of plumes located around the center of LLSVPs are usually vertical in the lower mantle but meander in the middle and upper mantle. Because of the physics included in the models, all MCs only have simple plume shape (without stagnation or meandering). They are always smooth curves extending from the LLSVPs to the surface hotspots. We will discuss this difference more in the next section.

The average seismic velocities of the TCs, MCs, and VCs are slower than the ambient mantle at all depths. TCs, however, are much slower than MCs and VCs. The average velocities of MCs are slower than the those along VCs only in the lower mantle (Figure 5a, f), which is consistent with the analysis of MCs and VCs done using older tomographic models (Boschi et al., 2007). The δV_S along MCs is often close to 0% or even positive in the upper mantle (Figure 3 and 4), while the δV_S along TCs is negative in most cases. There are a few exceptions in SEMUCB-WM1 (Cape Verde and San Felix) and GLAD-M25 (Azores, Canary, Hawaii, San Felix, Tahiti, and Tristan). In these cases, no CC can be identified at some depths in the upper mantle. This may indicate that the global tomographic model does not resolve the plume conduit at these depths. It is expected that plume radius can significantly decrease as a plume rising from the more viscous lower mantle to the less viscous upper mantle (Leng & Gurnis, 2012).

4.3 Implications of the slowness along plume conduits

The excess temperature of a purely thermal plume conduit is not expected to change significantly with depth since plumes rise rapidly relative to the thermal diffusion timescale and mantle heat production is negligible on the timescale of material ascent through a plume conduit. The exothermic phase transitions, for example, the olivine to wadsleyite transition at 410 km depth, and shear heating may be able to increase the temperature

of a plume, but they are secondary effects compared with the plume's inherent excess temperature. This implies that if a mantle plume is purely thermal, the amplitude of its δV_S should generally vary following the thermodynamically determined $d(\ln V_S)/dT$ profile with depth. Our observations from both tomographic models, however, show that the variation of δV_S along plume conduits almost never strictly follow the $d(\ln V_S)/dT$ profile, which suggests that non-thermal variations are present in plume conduits.

Non-thermal variations in mantle plumes include differences in intrinsic composition, water content, grain size, and melt fraction. At the 410 km discontinuity, the phase transition from wadsleyite to olivine may result in water release when plume materials rise and cross this boundary because wadsleyite has a higher water-bearing ability than olivine (W. Wang et al., 2019). Increasing water content can reduce V_S (C. Liu et al., 2023) and may cause partial melting in this region, further reducing V_S (Chantel et al., 2016). Isotopic measurements of OIBs and numerical models suggest that LLSVPs may be composed of a variety of different materials, ranging from primordial materials that get preserved at the CMB since the differentiation in early Earth's evolution (Labrosse et al., 2007; Deschamps et al., 2012) to piles of recycled oceanic crusts (Olson & Kincaid, 1991; Brandenburg & van Keken, 2007). For many of the traced conduits, we find that δV_S in the lowermost mantle is slower than expected on the basis of $d(\ln V_S)/dT$. The incorporation of compositionally-distinct material within the lowermost mantle is one possible explanation for the slower than expected velocities (Figure 3 and 4).

The systematically faster plumes (in the upper- and mid-mantle) originating from the African LLSVP than those originating from the Pacific LLSVP (Figure 5b, c, g, h) are consistent with previous estimates of plume excess temperature based on upper mantle wavespeed variations (Bao et al., 2022). Y. Wang and Wen (2007) and He and Wen (2009) also show that the two LLSVPs have different shape and topology. They may indicate that the two LLSVPs have different origins, but we cannot rule out the possibility that the faster plumes from the African LLSVP are caused by different seismic data coverage between the Pacific and the Atlantic regions.

4.4 Implications of diverse plume shapes

The shape of a plume conduit depends on both the plume's properties and its interaction with its surrounding mantle. Buoyancy, which is determined by $\Delta\rho$, the difference between the effective density of a plume and the density of its surrounding mantle ($\Delta\rho = \rho_{plume} - \rho_{mantle}$), controls the behaviours of a plume as it rises. The buoyant ascent of plume material and its interaction with the large-scale mantle flow will result in different plume conduit shapes. The composition of the plume, the pressure induced phase transitions, and the excess temperature (temperature difference between the potential temperature of a plume and the ambient mantle) together determine $\Delta\rho$. When a plume has a positive buoyancy ($\Delta\rho < 0$), it will rise, and it will start sinking when it has a negative buoyancy. When $\Delta\rho$ is close to or slightly smaller than 0, a plume could be ponded or develop a variety of complex shapes (Kumagai et al., 2008; Xiang et al., 2021).

The mantle viscosity structure and flow patterns of the ambient mantle also affect plume shapes. The mobility of a plume, that is how easily it gets deformed, is expected to be smaller in a more viscous than in a less viscous region (H. Liu & Leng, 2020). Large-scale mantle flows driven by thermal convection, surface plate motion, and subduction could shear plume conduits or largely deflect the secondary plume stemming from a ponding primary plume (Steinberger, 2000; Farnetani & Samuel, 2005).

The more complex shapes of our TCs than the MCs suggest that the mantle convection models used to determine MCs may not consider all major factors affecting plume shapes, especially in the mid-mantle across and below the mantle transition zone (MTZ), where plume ponding and large tilted angles are only observed in TCs.

First, the mid-mantle below the MTZ could have significant viscosity variations (Marquardt & Miyagi, 2015; Rudolph et al., 2015; Shim et al., 2017), which indicates a more complex rheology than the numerical models' assumption that only a few deformations occur and diffusion creep is predominant at these depths (Ferreira et al., 2019). Furthermore, the transition from ringwoodite to bridgmanite at 660 km, which can lead to plume ponding at this depth, is not considered neither. In return, the numerical models lack the ability to produce plumes that are ponded and deflected at different depths due to their simplified physics, which does not consider the composition variations, phase transitions, nor a temperature-dependent or strain-rate-dependent viscosity.

Second, the mantle flow field converted from the global tomographic model (Steinberger & O'Connell, 1998) may not be accurate at a smaller scale due to our current incomplete understanding of mantle dynamics. MCs are determined based on the assumption that a plume rose to the surface vertically within a short time and left a vertical 100-kilometer-radius conduit that gets passively advected by the large-scale mantle flows later. However, this assumption is only valid if mantle plumes are purely thermal. Recent seismic tomographic models have imaged plume conduits with a radius of ~ 500 km (S. French & Romanowicz, 2015) and much more complex morphology (Tsekhmistrenko et al., 2021; Celli et al., 2021; Wamba et al., 2023). Such broad plumes may not only be passively advected, but also influence the mantle flow field. Plumes with such large radius would have buoyancy fluxes that are much higher than previous estimations (Sleep, 1990; King & Adam, 2014). Together with the complex plume shapes, they suggest that many, if not all, mantle plumes are thermochemical rather than purely thermal. For example, a plume that incorporates an eclogitic component has a lower buoyancy flux and a larger radius than a purely thermal plume, which is more consistent with observations (Dannberg & Sobolev, 2015).

At ~ 410 km depth, previous numerical models suggest that plumes with some eclogitic component will have a buoyancy barrier due to the different phase transitions that occur in pyrolitic and eclogitic materials. This buoyancy barrier can result in plume ponding and the emergence of a secondary plume (Farnetani & Samuel, 2005; Dannberg & Sobolev, 2015). It can potentially explain the ponding of Samoa, a large tilted angle, and a large change in offset distance observed in SEMUCB-WM1 at this depth (Figure 6,9a).

Large tilted angles at 660 km depth mostly reflect plume ponding, which could be caused by the combined effect of the ~ 30-fold viscosity increase from above to below 660 km suggested by many geophysical studies (Hager, 1984; Mitrovica & Forte, 1997) as well as the endothermic phase transition from ringwoodite to bridgmanite (Faccenda & Dal Zilio, 2017). The phase transition can cause plume ponding as the hotter plume materials undergo this phase transition at a shallower depth, hindering ascent. Several scenarios may happen after a primary plume is ponded at this depth. First, the primary plume could penetrate the 660-discontinuity broadly while some plume materials are ponded. These ponding materials become so hot that there is a significant viscosity reduction, allowing the conduit to be laterally deflected by hundreds of kilometers (Tosi & Yuen, 2011). This scenario is observed for St. Helena and Tristan in both tomographic models (Figure 6, 7, 9b and S6).

When the primary plume cannot penetrate the 660-discontinuity in the first place, significant amount of plume materials will accumulate at this depth. The ponding materials will spread like a pancake and secondary plumes can develop from anywhere above the ponding zone. As a result, the offset distance between an upper-mantle secondary plume and a lower-mantle primary plume is not large, while the offset azimuth can be irrelevant to the flow patterns (Caroline in GLAD-M25, Azores, Iceland, Reunion in both tomographic models) (Figure 6, 7, 8c, 9c, S3 c and d). They may resemble the "plume-tree" model proposed in Liu and Leng (2020), which requires a thin low-viscosity layer beneath the 660 km ponding depth and a low-viscosity upper mantle to allow secondary plume(s) develop from any part of the ponding materials.

At a greater depth $\sim$ 1250 km, large tilted angles observed of Tahiti in both tomographic models, Hawaii in GLAD-M25, and Kerguelen in SEMUCB-WM1 (Figure 6) could arise if the viscosity is higher around this depth than in the mantle above and below it. Owing to the higher viscosity, conduits are less sheared around this depth, so the conduit above this depth could be preferentially deflected by mantle flow. Some inversions of geophysical data suggest that there exists a viscosity hump, a one-to-two-order of magnitude viscosity increase, between 800 and 1200 km depth (King & Masters, 1992; Mitrovica & Forte, 1997; Rudolph et al., 2015). Studies on mineral physics also suggest that the increasing strength of ferropericlase (Marquardt & Miyagi, 2015; Deng & Lee, 2017) and decreasing the iron-enrichment in bridgmanite (Shim et al., 2017) at the mid-mantle depth can both result in this mid-mantle viscosity hump.

Another mechanism that may produce large tilted angles at $\sim$ $1000 - 1250$ km (Canary and MacDonald in SEMUCB-WM1) is plume ponding and secondary plumes emerging. This mechanism is proposed by Wamba et al. (2023) to explain alternating vertical conduits and horizontal ponding zone observed for the Reunion and Comores plumes from $\sim$ 1000 km depth to the top of the asthenosphere in the latest tomographic models. There is no known endothermic phase transition, which could cause plume ponding, at these depths. However, a denser mantle below $\sim$ 1000 km depth due to its higher basalt content (Ballmer et al., 2015) could cause plume ponding at this depth if the thermal expansion effect is not strong enough to reduce the plume effective density to be smaller than the mantle density above $\sim$ 1000 km (Xiang et al., 2021). Seismic observations imply a not-global discontinuity presenting at 1000 km depth (Zhang et al., 2023), which may indicate a compositional layered mantle.

Other than these various behaviours of a single plume conduit, plume merging may further complicate the observed plume shapes. For example, we identify two CCs for Galapagos in the mid-mantle that merge into one CC with $< 1\%$ δV_S above 660 km in SEMUCB-WM1. It may represent that two adjacent conduits are ponded at 660 km and the ponding zones of them merge into one conduit or these two resolved CCs are caused by a lack of resolution in SEMUCB-WM1 as they are only observed in SEMUCB-WM1. The TCs of Macdonald and Pitcairn from GLAD-M25 suggest these two plumes merge in the mid-mantle and branch above 660 km. Merging of two adjacent plumes has been demonstrated by both lab experiment (Moses et al., 1991) and numerical models (e.g., Lewis-Merrill et al., 2022; Brunet & Yuen, 2000), and the branching of the merged conduit could be explained by secondary plumes emerging from a ponding plume.

Given all these uncertainties within our interpretations of plume dynamics from observed plume shapes, our TCs are useful for future numerical modeling. For example, idealized plume models can explore that under which geodynamics setting, the observed plume shapes can be reproduced. Our TCs can also provide a better schematic model for future studies to interpret the geochemical heterogeneity of OIBs from different hotspots. For example, previous studies have tried to interpret the heterogeneous isotopic signals of OIBs from neighbouring hotspots by correlating them with the vertical projection of the hotspots onto the CMB (Huang et al., 2011; Harpp & Weis, 2020) or interpreting these isotopic signals under simplified schematic plume models (Williams et al., 2019; Cordier et al., 2021). Our TCs can provide information about potential inter-plume interactions and the ascent history of plumes, which can be critical to the interpretations of geochemical observations.

5 Conclusion

Broad plumes clustering around LLSVPs have been recognized from the latest global tomographic models. Our study presents a systematic analysis of the pathways of these plume conduits. We carried out an analysis of the shapes of plume conduits in an immersive headset-based virtual reality (VR) environment. Our traced conduits from SEMUCB-

WM1 and GLAD-M25 appear to be slower than the conduits predicted by geodynamic models and vertical conduits regardless of whether they are evaluated in the same tomographic model or in a different tomographic model. This suggests that our manually-traced conduits are more consistent with the locus of slow seismic velocities within the mantle than either the vertical conduits that some authors have assumed when relating surface observables to deep mantle structures or the shapes of plume conduits predicted using physically simplified geodynamic models. Moreover, our traced conduits are more consistent with the petrologically-determined excess temperature than either of the other types of conduits.

In our manually traced conduits, the total amount of offset from the surface to the deep mantle is comparable between the traced and modeled conduits. However, our traced conduits reveal a tendency for plumes to stagnate or to be offset at mid-mantle depths, a behavior that is not captured in modeled conduits. Previous geophysical studies, mineral physics studies, and geodynamics modeling provide multiple mechanisms that could contribute to plume ponding or deflection, including the buoyancy barrier induced by phase transitions and the viscous decoupling of conduits. Our analysis of plume conduit shapes provides a dataset that can be of value across multiple disciplines including geodynamic modeling, geochemistry, and mineral physics.

6 Figures

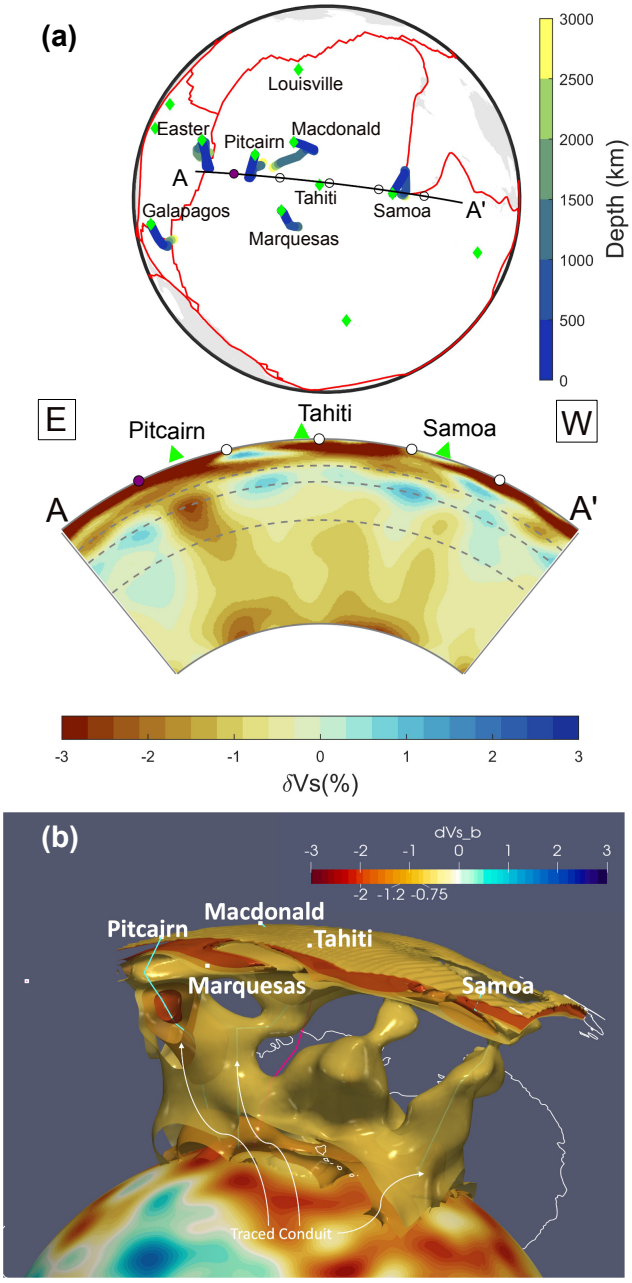

Figure 1. (a) Cross section of Pacific plumes in SEMUCB-WM1 and the location of the cross-section on the map, and (b) the 3D image of -2%, -1.2%, and -0.75% δV_S isosurfaces taken from the same region.

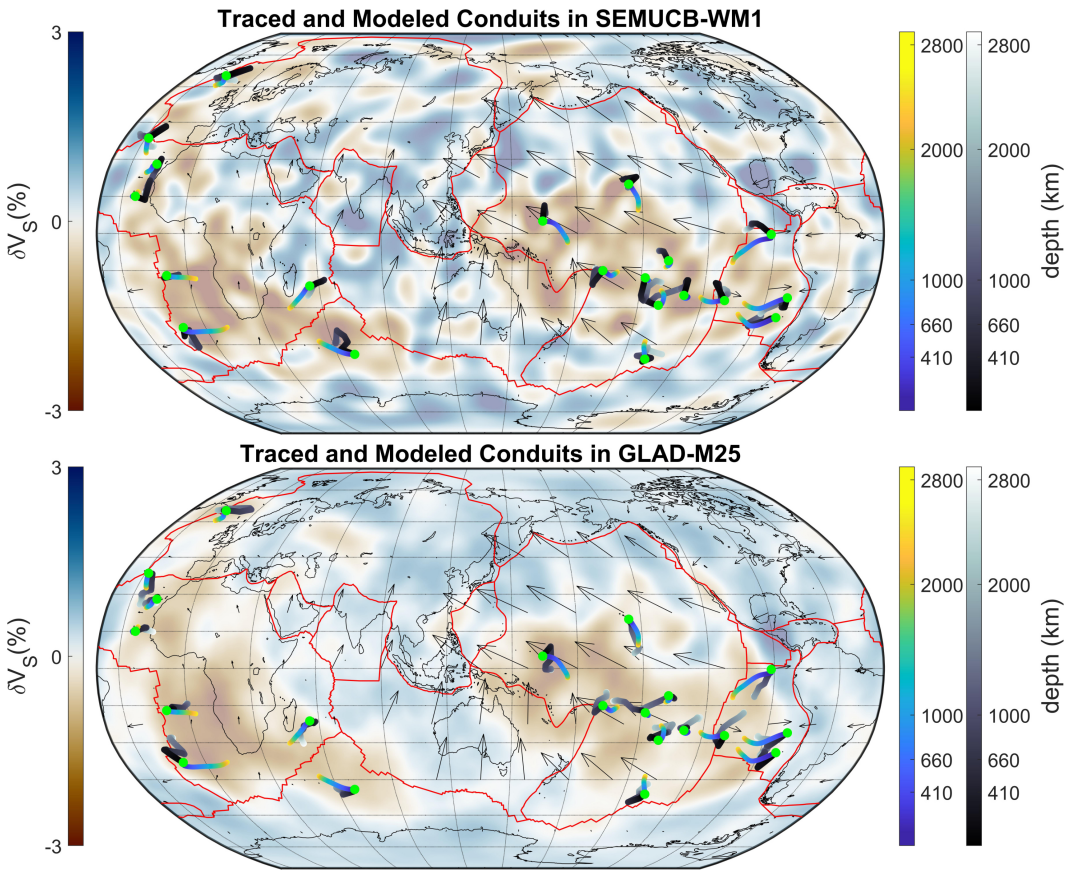

Figure 2. Map of dVs at 2850 km depth with 20 traced and numerical modeled (Steinberger & Antretter, 2006) plume conduits in SEMUCB-WM1 (top) and in GLAD-M25 (bottom). Colorful dots represent modeled ones, while black-white dots represent traced ones. Green circles represent the location of hotspots. The gray arrows represent plate motions in the spreading-aligned mantle reference frame of Becker et al. (2015).

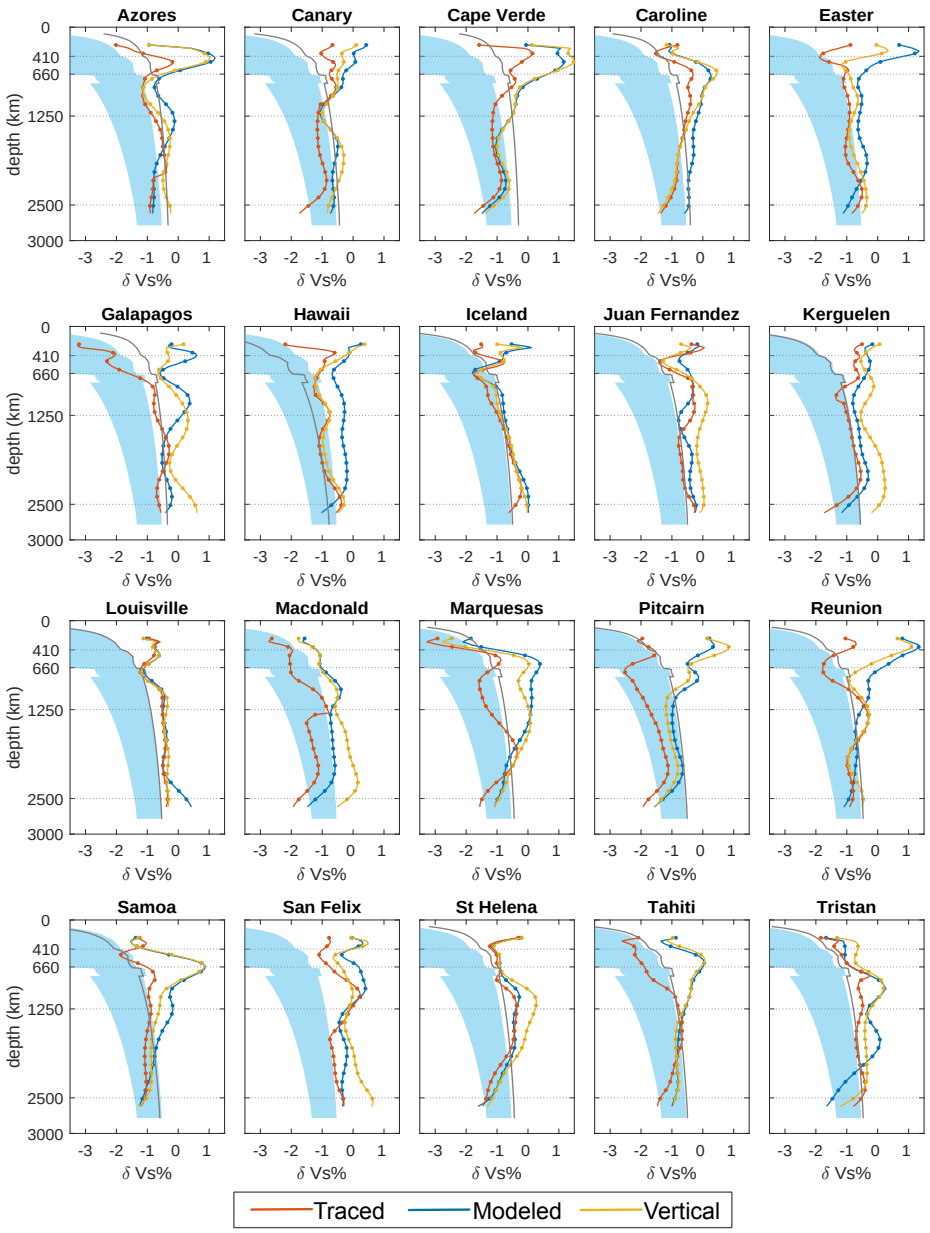

Figure 3. The depth profile of δV_S along 20 plume conduits in SEMUCB-WM1. Red represents the traced conduits. Blue represents the conduits modeled in Steinberger and Antretter (2006). Yellow represents the vertical conduits. The gray solid line is the corresponding δV_S of the petrologically estimated excess temperature from Putirka, 2008. The blue shade is the reference profile for expecting δV_S along a conduit given excess temperatures between 200 and 500 K calculated from the $d(\ln V_S)/dT$ profile (Figure. S1). δV_S magnitude along conduit can more likely be interpreted as the lower bound.

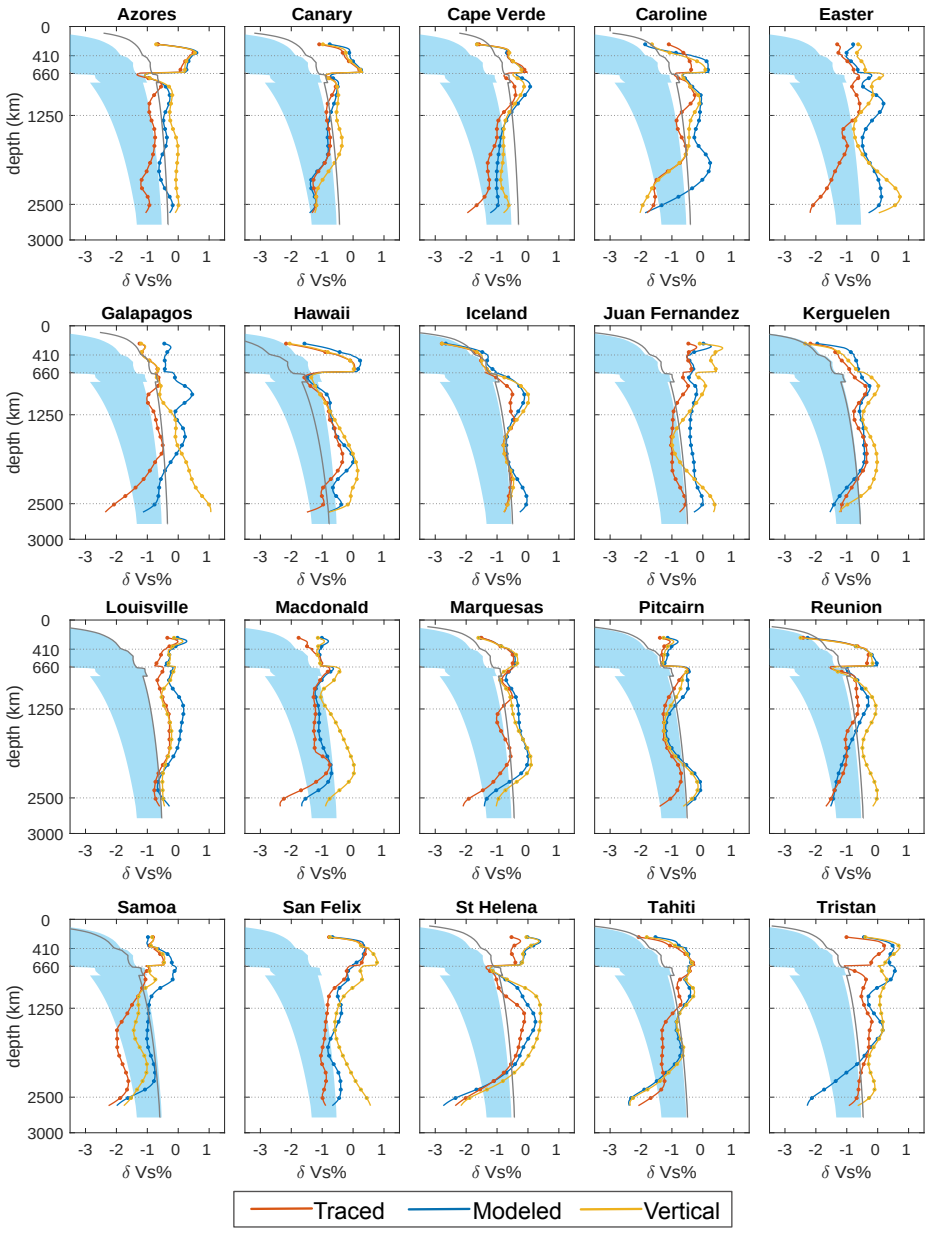

Figure 4. The depth profile of δV_S along 20 plume conduits in GLAD-M25 similar to Figure 3.

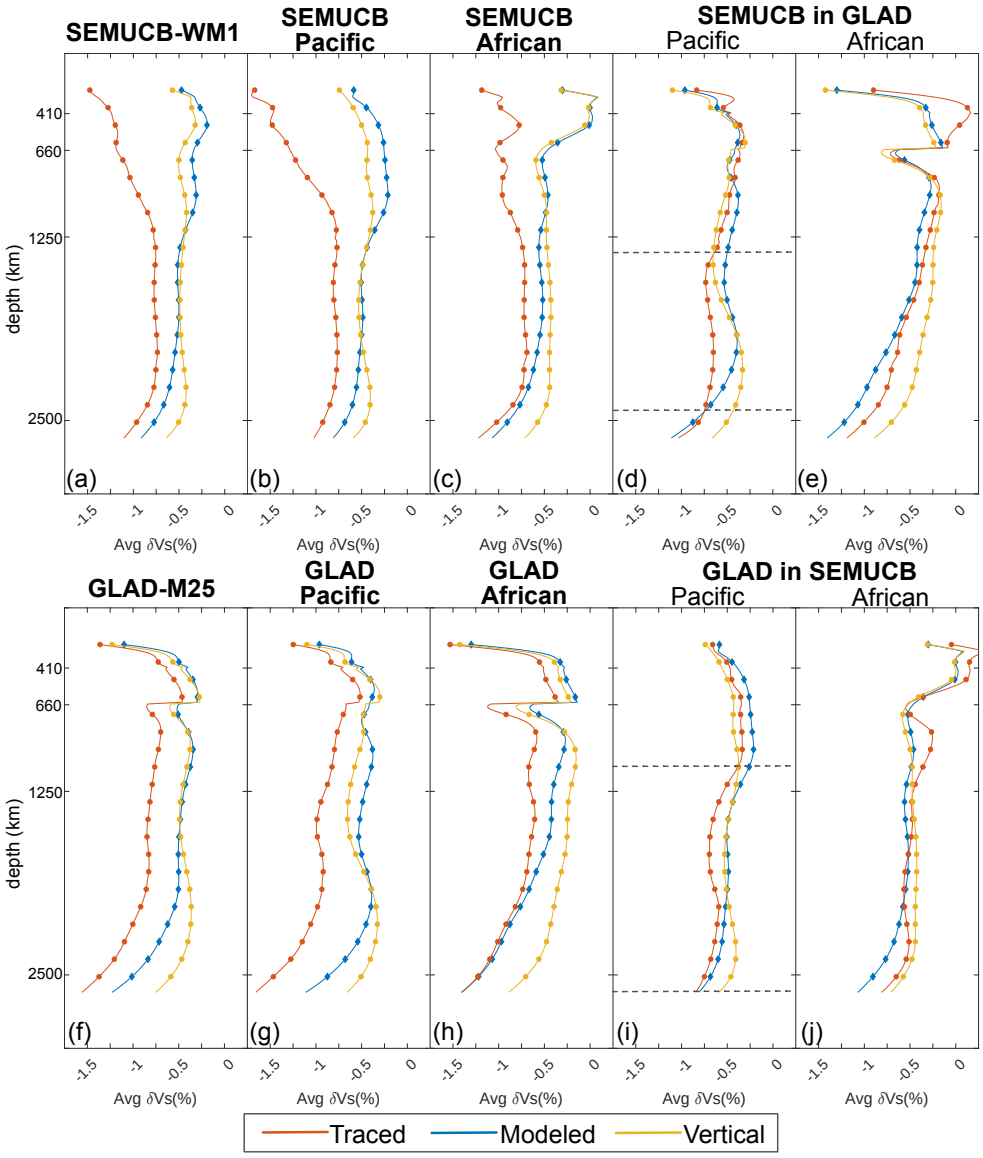

Figure 5. Average δV_S along traced, model-predicted, and vertical plume conduits in two tomographic models. Pacific plumes, which are plumes locate around the Pacific LLSVP, include Caroline, Easter, Galapagos, Hawaii, Macdonald, Marquesas, Pitcairn, Samoa, and Tahiti. African plumes, which are plumes locate around the African LLSVP, include Azores, Canary, Cape Verde, Iceland, Reunion, St. Helena, and Tristan. The dotted lines indicate the depth range where the traced plume conduits from SEMUCB-WM1 (GLAD-M25) outperform either the model-predicted or vertical plume conduits in GLAD-M25 (SEMUCB-WM1).

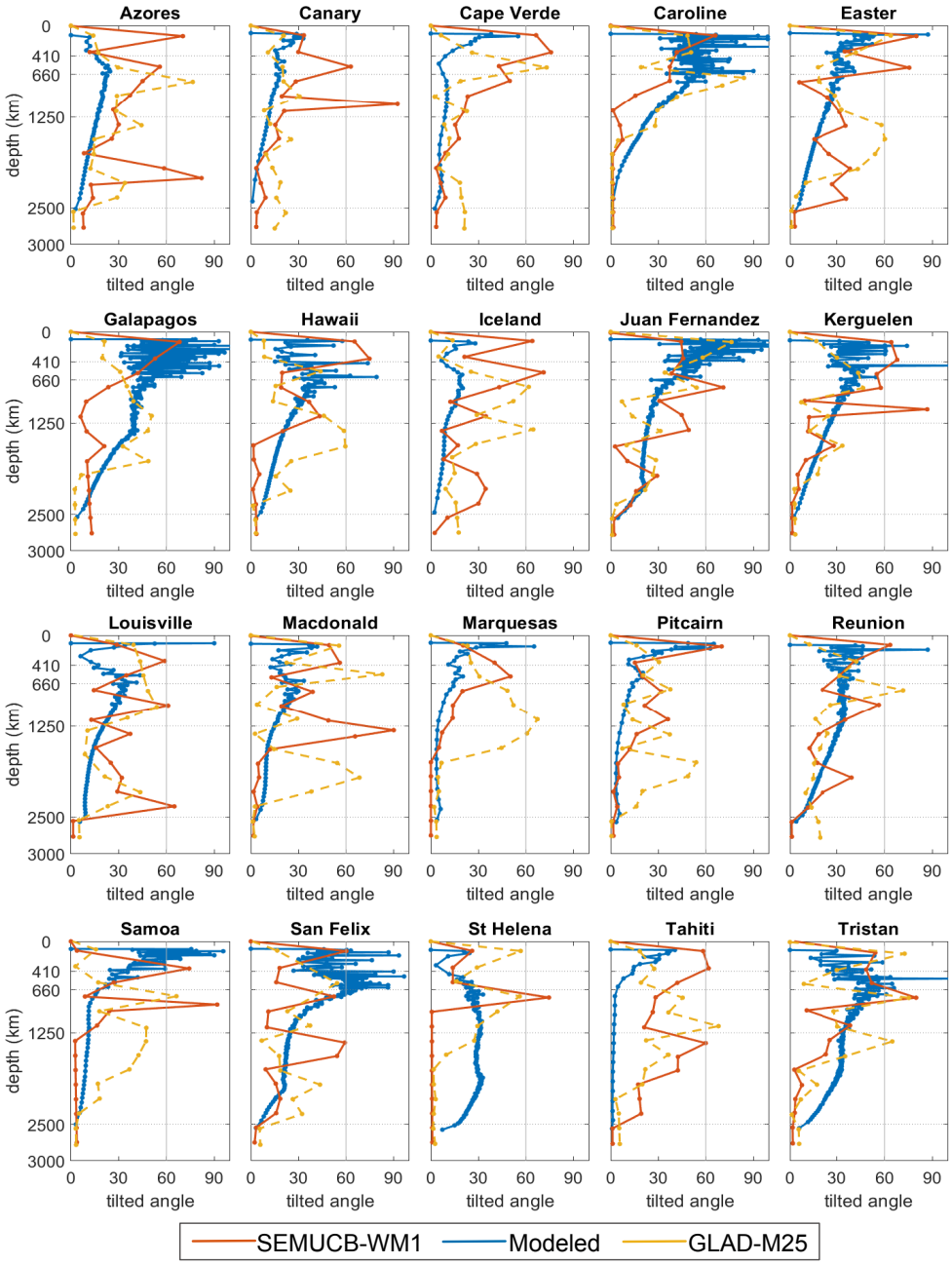

Figure 6. The depth profile of tilted angle along 20 plume conduits. Blue represents the conduits modeled in Steinberger and Antretter (2006). Red represents the traced conduits in SEMUCB-WM1. Yellow represents the traced conduits in GLAD-M25. The gray line marks the 60°angle.

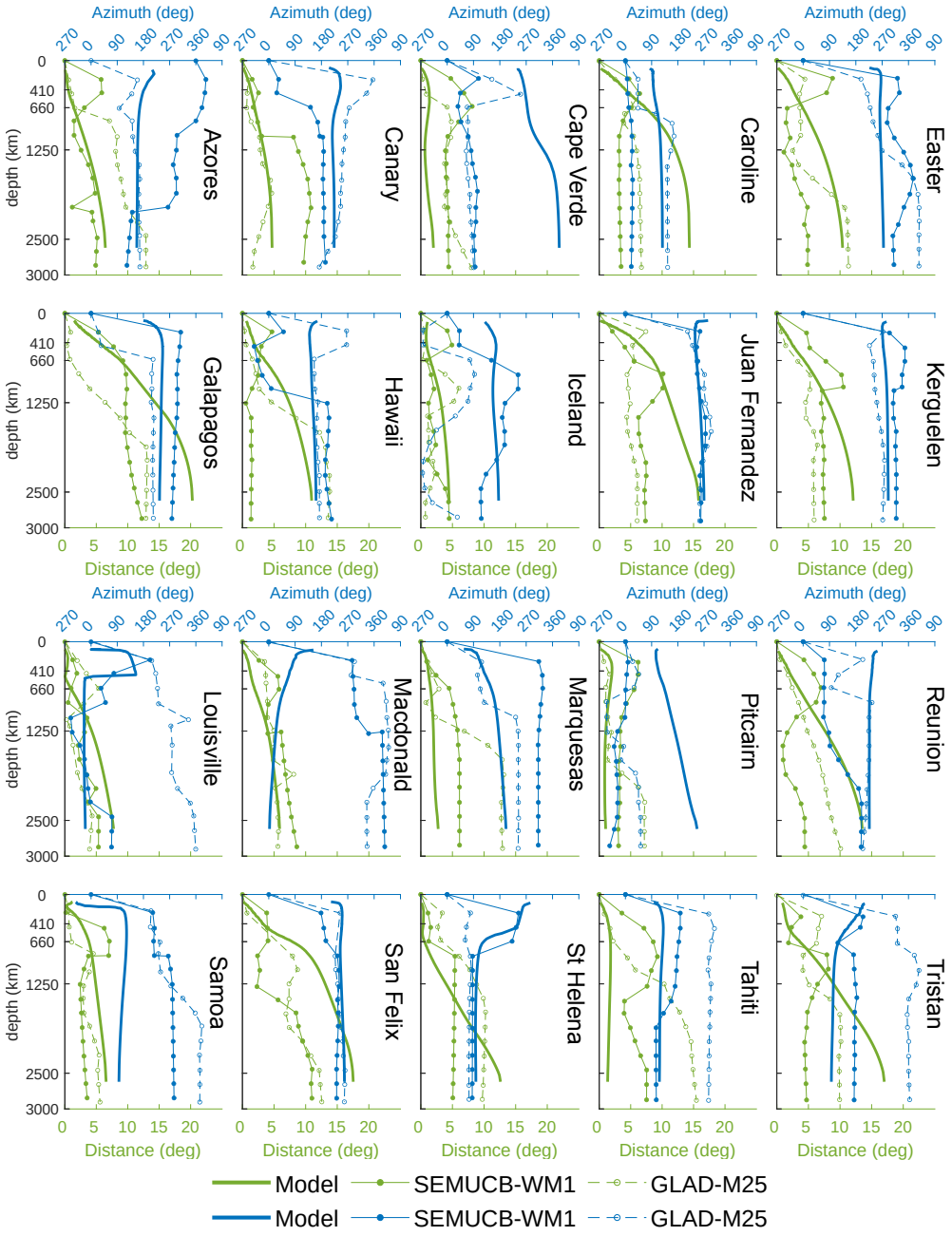

Figure 7. Azimuth and offset distance of model-predicted conduits and conduits traced in SEMUCB-WM1 and GLAD-M25 with respect to hotspots. Blue represents the azimuth of a conduit at different depths. Green represents the angular offset between a conduit and its hotspot.

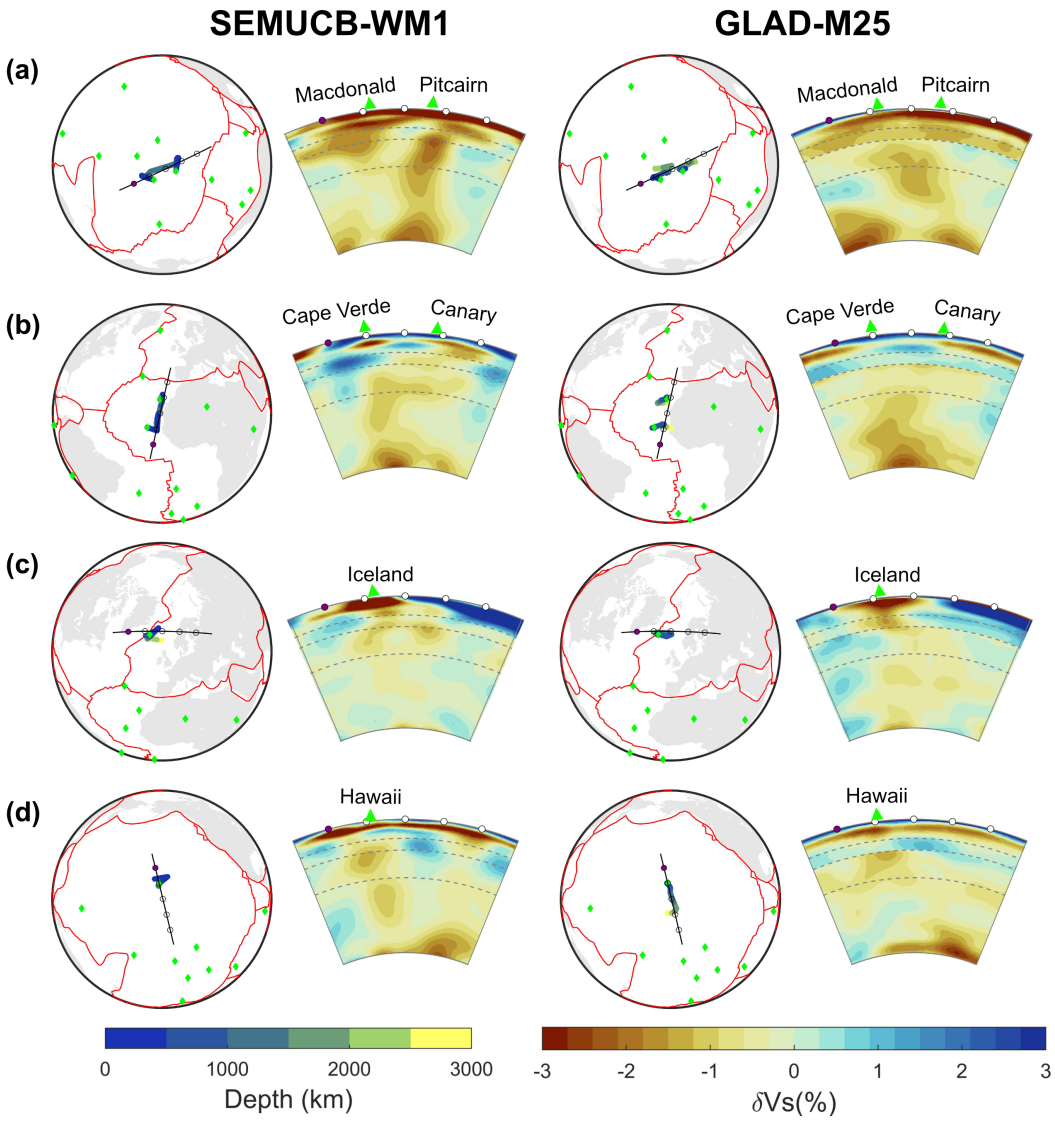

Figure 8. Cross section and map view of the traced conduits of a) Macdonald and Pitcairn, b) Cape Verde and Canary, c) Iceland, d) Hawaii in SEMUCB-WM1 and GLAD-M25. From top to bottom, the dash lines represent 410, 660, and 1250 km depth.

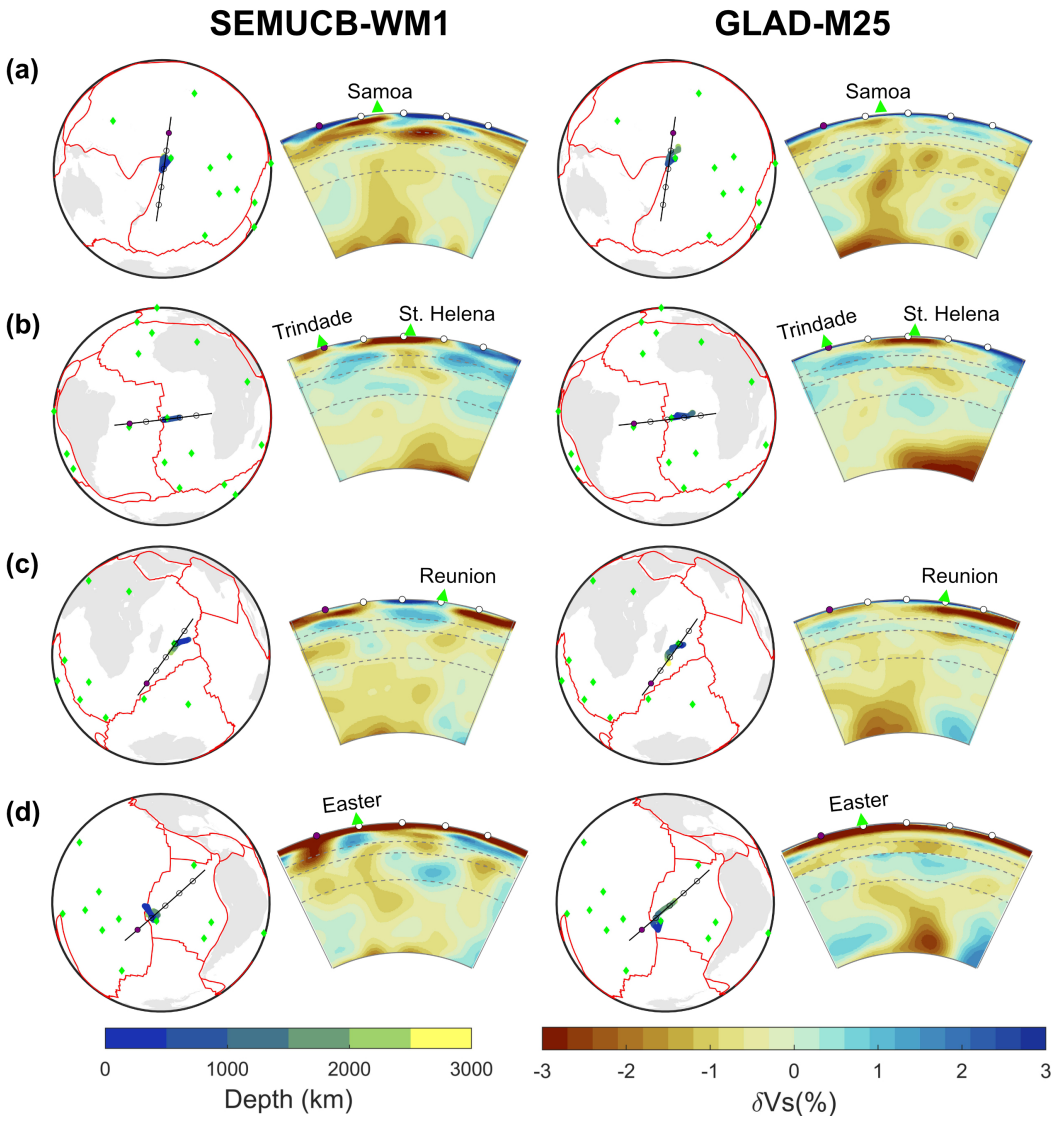

Figure 9. Cross section and map view of the traced conduits of a) Samoa, b) St Helena, c) Reunion, d) Easter similar to Figure 8

References

Ahrens, J., Geveci, B., & Law, C. (2005, January). 36 - ParaView: An End-User Tool for Large-Data Visualization. In C. D. Hansen & C. R. Johnson (Eds.), *Visualization Handbook* (pp. 717–731). Burlington: Butterworth-Heinemann. doi: 10.1016/B978-012387582-2/50038-1

Austermann, J., Kaye, B. T., Mitrovica, J. X., & Huybers, P. (2014, April). A statistical analysis of the correlation between large igneous provinces and lower mantle seismic structure. *Geophysical Journal International*, *197*(1), 1–9. doi: 10.1093/gji/ggt500

Ballmer, M. D., Schmerr, N. C., Nakagawa, T., & Ritsema, J. (2015, December). Compositional mantle layering revealed by slab stagnation at ˜1000-km depth. *Science Advances*, *1*(11), e1500815. doi: 10.1126/sciadv.1500815

Bao, X., Lithgow-Bertelloni, C. R., Jackson, M. G., & Romanowicz, B. (2022, January). On the relative temperatures of Earth's volcanic hotspots and mid-ocean ridges. *Science*, *375*(6576), 57–61. doi: 10.1126/science.abj8944

Bassin, C., Laske, G., & Masters, G. (2000, January). The current limits of resolution for surface wave tomography in North America. EOS Trans AGU 81:F897. *Eos*, *81*, F897.

Becker, T. W., Schaeffer, A. J., Lebedev, S., & Conrad, C. P. (2015). Toward a generalized plate motion reference frame. *Geophysical Research Letters*, *42*(9), 3188–3196. doi: 10.1002/2015GL063695

Billen, M. I., Kreylos, O., Hamann, B., Jadamec, M. A., Kellogg, L. H., Staadt, O., & Sumner, D. Y. (2008, September). A geoscience perspective on immersive 3D gridded data visualization. *Computers & Geosciences*, *34*(9), 1056–1072. doi: 10.1016/j.cageo.2007.11.009

Boschi, L., Becker, T. W., & Steinberger, B. (2007). Mantle plumes: Dynamic models and seismic images. *Geochemistry, Geophysics, Geosystems*, *8*(10). doi: 10.1029/2007GC001733

Brandenburg, J. P., & van Keken, P. E. (2007). Deep storage of oceanic crust in a vigorously convecting mantle. *Journal of Geophysical Research: Solid Earth*, *112*(B6). doi: 10.1029/2006JB004813

Brunet, D., & Yuen, D. A. (2000, May). Mantle plumes pinched in the transition zone. *Earth and Planetary Science Letters*, *178*(1), 13–27. doi: 10.1016/S0012-821X(00)00063-7

Celli, N. L., Lebedev, S., Schaeffer, A. J., & Gaina, C. (2021, September). The tilted Iceland Plume and its effect on the North Atlantic evolution and magmatism. *Earth and Planetary Science Letters*, *569*, 117048. doi: 10.1016/j.epsl.2021.117048

Chantel, J., Manthilake, G., Andrault, D., Novella, D., Yu, T., & Wang, Y. (2016, May). Experimental evidence supports mantle partial melting in the asthenosphere. *Science Advances*, *2*(5), e1600246. doi: 10.1126/sciadv.1600246

Cordier, C., Delavault, H., & Chauvel, C. (2021, August). Geochemistry of the Society and Pitcairn-Gambier mantle plumes: What they share and do not share. *Geochimica et Cosmochimica Acta*, *306*, 362–384. doi: 10.1016/j.gca.2021.04.014

Courtillot, V., Davaille, A., Besse, J., & Stock, J. (2003, January). Three distinct types of hotspots in the Earth's mantle. *Earth and Planetary Science Letters*, *205*(3), 295–308. doi: 10.1016/S0012-821X(02)01048-8

Dannberg, J., & Sobolev, S. V. (2015, April). Low-buoyancy thermochemical plumes resolve controversy of classical mantle plume concept. *Nature Communications*, *6*(1), 6960. doi: 10.1038/ncomms7960

Davaille, A., & Romanowicz, B. (2020). Deflating the LLSVPs: Bundles of Mantle Thermochemical Plumes Rather Than Thick Stagnant "Piles". *Tectonics*, *39*(10), e2020TC006265. doi: 10.1029/2020TC006265

Davies, D. R., Goes, S., & Sambridge, M. (2015, February). On the relationship between volcanic hotspot locations, the reconstructed eruption sites of large igneous provinces and deep mantle seismic structure. *Earth and Planetary Science Letters*, *411*, 121–130. doi: 10.1016/j.epsl.2014.11.052

Deng, J., & Lee, K. K. M. (2017, December). Viscosity jump in the lower mantle inferred from melting curves of ferropericlase. *Nature Communications*, *8*(11), 1997. doi: 10.1038/s41467-017-02263-z

Deschamps, F., Cobden, L., & Tackley, P. J. (2012, October). The primitive nature of large low shear-wave velocity provinces. *Earth and Planetary Science Letters*, *349-350*, 198–208. doi: 10.1016/j.epsl.2012.07.012

Doubrovine, P. V., Steinberger, B., & Torsvik, T. H. (2016). A failure to reject: Testing the correlation between large igneous provinces and deep mantle structures with edf statistics. *Geochemistry, Geophysics, Geosystems*, *17*(3), 1130–1163. doi: 10.1002/2015GC006044

Faccenda, M., & Dal Zilio, L. (2017, January). The role of solid–solid phase transitions in mantle convection. *Lithos*, *268-271*, 198–224. doi: 10.1016/j.lithos.2016.11.007

Farnetani, C. G., & Samuel, H. (2005). Beyond the thermal plume paradigm. *Geophysical Research Letters*, *32*(7). doi: 10.1029/2005GL022360

Ferreira, A. M. G., Faccenda, M., Sturgeon, W., Chang, S.-J., & Schardong, L. (2019, April). Ubiquitous lower-mantle anisotropy beneath subduction zones. *Nature Geoscience*, *12*(4), 301–306. doi: 10.1038/s41561-019-0325-7

French, S., Lekic, V., & Romanowicz, B. (2013, October). Waveform tomography reveals channeled flow at the base of the oceanic asthenosphere. *Science*, *342*(6155), 227–230. doi: 10.1126/science.1241514

French, S., & Romanowicz, B. (2015, September). Broad plumes rooted at the base of the Earth's mantle beneath major hotspots. *Nature*, *525*(7567), 95–99. doi: 10.1038/nature14876

French, S. W., & Romanowicz, B. A. (2014, December). Whole-mantle radially anisotropic shear velocity structure from spectral-element waveform tomography. *Geophysical Journal International*, *199*(3), 1303–1327. doi: 10.1093/gji/ggu334

Hager, B. H. (1984). Subducted slabs and the geoid: Constraints on mantle rheology and flow. *Journal of Geophysical Research: Solid Earth*, *89*(B7), 6003–6015. doi: 10.1029/JB089iB07p06003

Harpp, K. S., & Weis, D. (2020). Insights Into the Origins and Compositions of Mantle Plumes: A Comparison of Galápagos and Hawai'i. *Geochemistry, Geophysics, Geosystems*, *21*(9), e2019GC008887. doi: 10.1029/2019GC008887

Hassan, R., Flament, N., Gurnis, M., Bower, D. J., & Müller, D. (2015). Provenance of plumes in global convection models. *Geochemistry, Geophysics, Geosystems*, *16*(5), 1465–1489. doi: 10.1002/2015GC005751

He, Y., & Wen, L. (2009). Structural features and shear-velocity structure of the "Pacific Anomaly". *Journal of Geophysical Research: Solid Earth*, *114*(B2). doi: 10.1029/2008JB005814

Huang, S., Hall, P. S., & Jackson, M. G. (2011, December). Geochemical zoning of volcanic chains associated with Pacific hotspots. *Nature Geoscience*, *4*(12), 874–878. doi: 10.1038/ngeo1263

Jackson, M. G., Becker, T. W., & Steinberger, B. (2021). Spatial Characteristics of Recycled and Primordial Reservoirs in the Deep Mantle. *Geochemistry, Geophysics, Geosystems*, *22*(3), e2020GC009525. doi: 10.1029/2020GC009525

King, S. D., & Adam, C. (2014, October). Hotspot swells revisited. *Physics of the Earth and Planetary Interiors*, *235*, 66–83. doi: 10.1016/j.pepi.2014.07.006

King, S. D., & Masters, G. (1992). An inversion for radial viscosity structure using seismic tomography. *Geophysical Research Letters*, *19*(15), 1551–1554. doi: 10.1029/92GL01700

Kumagai, I., Davaille, A., Kurita, K., & Stutzmann, E. (2008). Mantle plumes: Thin, fat, successful, or failing? Constraints to explain hot spot volcanism through time and space. *Geophysical Research Letters*, *35*(16). doi: 10.1029/2008GL035079

Kustowski, B., Ekström, G., & Dziewoński, A. M. (2008). Anisotropic shear-wave velocity structure of the Earth's mantle: A global model. *Journal of Geophysical Research: Solid Earth*, *113*(B6). doi: 10.1029/2007JB005169

Labrosse, S., Hernlund, J. W., & Coltice, N. (2007, December). A crystallizing dense magma ocean at the base of the Earth's mantle. *Nature*, *450*(7171), 866–869. doi: 10.1038/nature06355

Lei, W., Ruan, Y., Bozdağ, E., Peter, D., Lefebvre, M., Komatitsch, D., ... Pugmire, D. (2020, October). Global adjoint tomography—model GLAD-M25. *Geophysical Journal International*, *223*(1), 1–21. doi: 10.1093/gji/ggaa253

Leng, W., & Gurnis, M. (2012). Shape of thermal plumes in a compressible mantle with depth-dependent viscosity. *Geophysical Research Letters*, *39*(5). doi: http://dx.doi.org/10.1029/2012GL050959

Lewis-Merrill, J., Lo, W. K., Agarwal, K., & Lithgow-Bertelloni, C. R. (2022, December). Do Mantle Plumes Merge? In *Agu fall meeting abstracts* (Vol. 2022, p. DI53A-03).

Liu, C., Yoshino, T., Yamazaki, D., Tsujino, N., Gomi, H., Sakurai, M., ... Higo, Y. (2023, August). Effect of water on seismic attenuation of the upper mantle: The origin of the sharp lithosphere–asthenosphere boundary. *Proceedings of the National Academy of Sciences*, *120*(32), e2221770120. doi: 10.1073/pnas.2221770120

Liu, H., & Leng, W. (2020). Plume -Tree Structure Induced by Low-Viscosity Layers in the Upper Mantle. *Geophysical Research Letters*, *47*(1), e2019GL086508. doi: 10.1029/2019GL086508

Marquardt, H., & Miyagi, L. (2015, April). Slab stagnation in the shallow lower mantle linked to an increase in mantle viscosity. *Nature Geoscience*, *8*(4), 311–314. doi: 10.1038/ngeo2393

Matthews, K. J., Maloney, K. T., Zahirovic, S., Williams, S. E., Seton, M., & Müller, R. D. (2016, November). Global plate boundary evolution and kinematics since the late Paleozoic. *Global and Planetary Change*, *146*, 226–250. doi: 10.1016/j.gloplacha.2016.10.002

Mitrovica, J. X., & Forte, A. M. (1997). Radial profile of mantle viscosity: Results from the joint inversion of convection and postglacial rebound observables. *Journal of Geophysical Research: Solid Earth*, *102*(B2), 2751–2769. doi: 10.1029/96JB03175

Moses, E., Zocchi, G., Procaccia, I., & Libchaber, A. (1991, January). The Dynamics and Interaction of Laminar Thermal Plumes. *Europhysics Letters*, *14*(1), 55. doi: 10.1209/0295-5075/14/1/010

Mégnin, C., & Romanowicz, B. (2000, December). The three-dimensional shear velocity structure of the mantle from the inversion of body, surface and higher-mode waveforms. *Geophysical Journal International*, *143*(3), 709–728. doi: 10.1046/j.1365-246X.2000.00298.x

Olson, P., & Kincaid, C. (1991). Experiments on the interaction of thermal convection and compositional layering at the base of the mantle. *Journal of Geophysical Research: Solid Earth*, *96*(B3), 4347–4354. doi: 10.1029/90JB02530

Putirka, K. (2008, April). Excess temperatures at ocean islands: Implications for mantle layering and convection. *Geology*, *36*(4), 283–286. doi: 10.1130/G24615A.1

Richards, M. A., Duncan, R. A., & Courtillot, V. E. (1989, October). Flood Basalts and Hot-Spot Tracks: Plume Heads and Tails. *Science*, *246*(4926), 103–107. doi: 10.1126/science.246.4926.103

Rudolph, M. L., Lekić, V., & Lithgow-Bertelloni, C. (2015, December). Viscosity

jump in Earth's mid-mantle. *Science*, *350*(6266), 1349–1352. doi: 10.1126/science.aad1929

Shim, S.-H., Grocholski, B., Ye, Y., Alp, E. E., Xu, S., Morgan, D., ... Prakapenka, V. B. (2017, June). Stability of ferrous-iron-rich bridgmanite under reducing midmantle conditions. *Proceedings of the National Academy of Sciences*, *114*(25), 6468–6473. doi: 10.1073/pnas.1614036114

Sleep, N. H. (1990). Hotspots and mantle plumes: Some phenomenology. *Journal of Geophysical Research: Solid Earth*, *95*(B5), 6715–6736. doi: 10.1029/JB095iB05p06715

Steinberger, B. (2000). Plumes in a convecting mantle: Models and observations for individual hotspots. *Journal of Geophysical Research: Solid Earth*, *105*(B5), 11127–11152. doi: 10.1029/1999JB900398

Steinberger, B., & Antretter, M. (2006). Conduit diameter and buoyant rising speed of mantle plumes: Implications for the motion of hot spots and shape of plume conduits. *Geochemistry, Geophysics, Geosystems*, *7*(11). doi: 10.1029/2006GC001409

Steinberger, B., & O'Connell, R. J. (1998). Advection of plumes in mantle flow: implications for hotspot motion, mantle viscosity and plume distribution. *Geophysical Journal International*, *132*(2), 412–434. doi: 10.1046/j.1365-246x.1998.00447.x

Steinberger, B., & Torsvik, T. H. (2012). A geodynamic model of plumes from the margins of Large Low Shear Velocity Provinces. *Geochemistry, Geophysics, Geosystems*, *13*(1). doi: 10.1029/2011GC003808

Tan, E., Leng, W., Zhong, S., & Gurnis, M. (2011). On the location of plumes and lateral movement of thermochemical structures with high bulk modulus in the 3-D compressible mantle. *Geochemistry, Geophysics, Geosystems*, *12*(7). doi: 10.1029/2011GC003665

Torsvik, T. H., Smethurst, M. A., Burke, K., & Steinberger, B. (2006, December). Large igneous provinces generated from the margins of the large low-velocity provinces in the deep mantle. *Geophysical Journal International*, *167*(3), 1447–1460. doi: 10.1111/j.1365-246X.2006.03158.x

Tosi, N., & Yuen, D. A. (2011, December). Bent-shaped plumes and horizontal channel flow beneath the 660km discontinuity. *Earth and Planetary Science Letters*, *312*(3), 348–359. doi: 10.1016/j.epsl.2011.10.015

Tsekhmistrenko, M., Sigloch, K., Hosseini, K., & Barruol, G. (2021, August). A tree of Indo-African mantle plumes imaged by seismic tomography. *Nature Geoscience*, *14*(8), 612–619. doi: 10.1038/s41561-021-00762-9

Wamba, M. D., Montagner, J.-P., & Romanowicz, B. (2023, January). Imaging deep-mantle plumbing beneath La Réunion and Comores hot spots: Vertical plume conduits and horizontal ponding zones. *Science Advances*, *9*(4), eade3723. doi: 10.1126/sciadv.ade3723

Wamba, M. D., Montagner, J.-P., Romanowicz, B., & Barruol, G. (2021). Multi-Mode Waveform Tomography of the Indian Ocean Upper and Mid-Mantle Around the Réunion Hotspot. *Journal of Geophysical Research: Solid Earth*, *126*(8), e2020JB021490. doi: 10.1029/2020JB021490

Wang, W., Walter, M. J., Peng, Y., Redfern, S., & Wu, Z. (2019, August). Constraining olivine abundance and water content of the mantle at the 410-km discontinuity from the elasticity of olivine and wadsleyite. *Earth and Planetary Science Letters*, *519*, 1–11. doi: 10.1016/j.epsl.2019.04.018

Wang, Y., & Wen, L. (2007). Geometry and P and S velocity structure of the "African Anomaly". *Journal of Geophysical Research: Solid Earth*, *112*(B5). doi: 10.1029/2006JB004483

Williams, C. D., Mukhopadhyay, S., Rudolph, M. L., & Romanowicz, B. (2019). Primitive Helium Is Sourced From Seismically Slow Regions in the Lowermost Mantle. *Geochemistry, Geophysics, Geosystems*, *20*(8), 4130–4145. doi:

10.1029/2019GC008437

Xiang, G., Wang, Z., & Kusky, T. M. (2021, December). Density and viscosity changes between depleted and primordial mantle at ∼1000 km depth influence plume upwelling behavior. *Earth and Planetary Science Letters*, *576*, 117213. doi: 10.1016/j.epsl.2021.117213

Zhang, Z., Irving, J. C. E., Simons, F. J., & Alkhalifah, T. (2023, March). Seismic evidence for a 1000 km mantle discontinuity under the Pacific. *Nature Communications*, *14*(1), 1714. doi: 10.1038/s41467-023-37067-x

Open Research Section

The data and computer code necessary to reproduce all figures is available on Zenodo (doi: 10.5281/zenodo.10668212). 3D-visulization is done using the Paraview 5.10.0 (Ahrens et al., 2005) visualization software.

Acknowledgments

The authors acknowledge support from NSF CSEDI grant EAR-1800450, NSF FRES grant EAR-2317937 and UC Davis. The authors thank UC Davis and the KeckCAVES data lab residing in this institution for allowing the authors to use the VR headsets in the lab. The authors are grateful of Oliver Kreylos and Sarah King for their assistance with the VR environment. The authors also thank Barbara Romanowicz for helpful discussions about this work.